Multimodal optical imaging and modulation through Smart Dura in non-human primates

Nari Hong[1,2], Sergio Montalvo Vargo[3], Gaku Hatanaka[2,4], Zhaoyu Gong[1], Noah Stanis[1,2], Jasmine Zhou[1,2], Tiphaine Belloir[1,2], Ruikang K Wang[1], Wyeth Bair[2,4], Maysamreza Chamanzar[3,5,6*], Azadeh Yazdan-Shahmorad[1,2,7,8*]

1. Department of Bioengineering, University of Washington, Seattle, WA, 98195, USA.

2. Washington National Primate Research Center, Seattle, WA, 98195, USA.

3. Department of Electrical and Computer Engineering, Carnegie Mellon University, Pittsburgh, PA, 15213, USA.

4. Department of Neurobiology and Biophysics, University of Washington, Seattle, WA, 98195, USA.

5. Department of Biomedical Engineering, Carnegie Mellon University, Pittsburgh, PA, 15213, USA.

6. Carnegie Mellon Neuroscience Institute, Pittsburgh, PA, 15213, USA.

7. Department of Electrical and Computer Engineering, University of Washington, Seattle, WA, 98195, USA.

8. Weill Neurohub

*Correspondence: mchamanzar@cmu.edu and azadehy@uw.edu

Abstract

A multimodal neural interface integrating electrical and optical functionalities is a promising tool for recording and manipulating neuronal activity, providing multiscale information with enhanced spatiotemporal resolution. However, most technologies for multimodal implementation are limited in their applications to small animal models and lack the ability to translate to larger brains, such as non-human primates (NHPs). Recently, we have developed a large-scale neural interface for NHPs, Smart Dura, which enables electrophysiological recordings and high optical accessibility. In this paper, we demonstrate the multimodal applications of Smart Dura in NHPs by combining with multiphoton imaging, optical coherence tomography angiography (OCTA), and intrinsic signal optical imaging (ISOI), as well as optical manipulations such as photothrombotic lesioning and optogenetics. Through the transparent Smart Dura, we could obtain fluorescence images down to 200 μm and 550 μm depth using two-photon and three-photon microscopy, respectively. Integrated with simultaneous electrophysiology using the Smart Dura, we could also assess vascular and neural dynamics with OCTA and ISOI, induce ischemic stroke, and apply optogenetic neuromodulation over a wide coverage area of 20 mm diameter. This multimodal interface enables comprehensive investigations of brain dynamics in NHPs, advancing translational neurotechnology for human applications.

Introduction

Brain mapping is a long-standing challenge in neuroscience research. As tools for studying neural circuits at multiple spatial and temporal scales, various neurotechnologies have been developed to record and manipulate neuronal activity, based on two main modalities: electrical or optical[1]. Electrical interfaces, such as penetrating probes and electrocorticography (ECoG), are capable of electrophysiological recording and stimulation with high temporal resolution but lack spatial precision. On the other hand, optical techniques, such as fluorescence calcium imaging and intrinsic signal imaging, enable structural and functional imaging with high spatial resolution but have difficulty in detecting fast neuronal activity. In addition, optical manipulations, such as optogenetics[2], facilitate cell-type specific neuromodulation but require genetic modification. A multimodal interface that offers the advantages of these individual functionalities can be a powerful tool for integrating complementary information with unprecedented spatiotemporal resolution; however, most studies still rely on a single modality, as it is challenging to apply optical approaches to conventional electrical interfaces, typically made of rigid and opaque materials.

Recent advances in implementing multimodal integration have focused on developing flexible and transparent neural interfaces and combining these with various optical imaging and manipulations[3–5]. To

fabricate multimodal interfaces, flexible polymers such as polyimide, polyethylene terephthalate, parylene C, and polydimethylsiloxane (PDMS) have been used as substrates. Moreover, transparent materials such as graphene, indium tin oxide, carbon nanotubes, and PEDOT:PSS have been employed as electrodes to further enhance optical transparency. Using the developed interfaces, previous studies have demonstrated intracortical[6] or surface[7–10] recordings combined with wide-field or two-photon calcium imaging. In addition, simultaneous electrophysiological recording and optical imaging have been attempted in conjunction with voltage-sensitive dye imaging[11] and intrinsic signal imaging[12]. Furthermore, the application of optogenetic modulation and recording of the corresponding electrophysiological responses has also been shown[9,13–15] Despite these significant recent efforts, most techniques are still limited in their applications to small animal models, such as rodents. To ultimately be applicable and translatable to humans, the interface needs to be scaled up to allow recording and imaging over wider coverage areas as well as neuromodulation across larger volumes. Moreover, this needs to be validated in larger brains, such as non-human primates (NHPs), as they can bring relevant translational insights with their high cognitive and behavioral complexity[16,17].

We recently developed a large-scale multimodal neural interface for NHPs, called Smart Dura[18]. Smart Dura is a functional version of an artificial dura[19–22] that can replace the native dura, providing electrophysiological recordings and high optical accessibility to large cortical areas. Following our previous work focusing on the fabrication and validating electrophysiology capability, in this study, we present the potential of Smart Dura for optical imaging and manipulation applications (Fig. 1a). We demonstrate the feasibility of combining the Smart Dura with multiphoton imaging, optical coherence tomography angiography (OCTA), and intrinsic signal optical imaging (ISOI), which are utilized to assess neural and vascular functions. We also show that two optical manipulations for modulating vascular and neural dynamics, photothrombotic lesioning and optogenetics, can be applied to neural recording using Smart Dura.

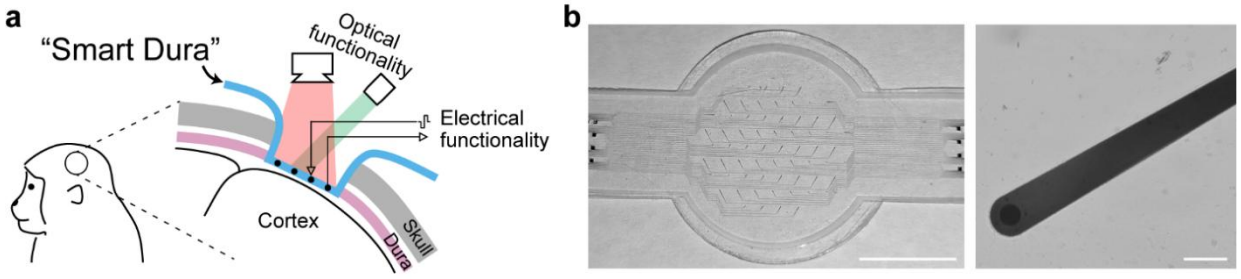

Fig. 1. Smart Dura as a large-scale multimodal neural interface. (a) Schematic illustration of electrical and optical functionalities of Smart Dura. (b) Photograph of the Smart Dura and micrograph of the electrode. Scale bar: 10 mm and 50 μm.

Results

A Smart Dura[18] is a large-scale functional artificial dura for NHPs with several key components. First, it is a μECoG array fabricated on biocompatible, flexible, and transparent PDMS that replicates the mechanical properties of native dura and achieves optical access to the brain. In previous studies, it was shown that an artificial dura made of this silicone polymer offered a long-term stable optical port by replacing the native dura[22–25]. Second, it is a surface electrode array that promises minimal invasiveness and larger cortical coverage. Lastly, it has micro-sized electrodes and traces, allowing for enhanced optical transparency and the potential to measure highly localized high-frequency activity, including single- or multi-unit activity[26]. Here, we used a Smart Dura with 64 microelectrodes, each with a diameter of 20 μm as shown in Fig. 1b. The 64-channel Smart Dura was placed directly on the surface of the cortex by removing the native dura to record subdural local field potentials (LFPs) in combination with optical imaging and manipulations.

Multiphoton imaging through the transparent Smart Dura

To validate the optical transparency and imaging capability of our Smart Dura, we performed multiphoton imaging both bench-side and in vivo. Multiphoton microscopy has been used for structural and functional deep brain imaging, including NHPs[27,28]. Using two-photon microscopy with 920 nm excitation light, we first imaged a fluorescence pollen sample, which contains grains with a diameter of tens of micrometers similar to neurons, placed under the Smart Dura (Fig. 2a). The electrode of Smart Dura was facing downward toward the fluorescent sample, mimicking the brain imaging with simultaneous electrical recording. As shown in a 3D multi-stack image in Fig. 2a, fluorescence from the pollen grains was successfully detected through the transparent layers of the Smart Dura. Moreover, grains below opaque metal traces could also be detected. In the bottom stack image in Fig. 2b, a shadow was observed under the widest trace of the electrode opening site, which is 50 μm wide, however, the loss of fluorescence intensity was almost negligible below the 10 μm-wide narrow trace.

Next, we conducted in vivo multiphoton imaging of cortical vasculature through the Smart Dura using intravenously administered FITC-dextran in the anesthetized animal. With two-photon microscopy, we could obtain fluorescence images of microvasculature in the primary visual cortex (V1) through the Smart Dura at depths of up to 200 μm (Fig. 2b). As shown in intensity profiles in Fig. 2c, the widest trace with a width of 50 μm resulted in a significant intensity reduction at 100 μm depth, but only a slight decrease at 200 μm depth. On the other hand, the 10 μm-wide narrow trace had little effect on the intensity at both depths of 100 μm and 200 μm. We next acquired vascular images using three-photon microscopy with 1300 nm excitation light, which is commonly used to image deeper brain regions[29,30], and were able to image microvasculature at depths of up to 550 μm (Fig. 2d). The metal trace of 10 μm cast negligible shadows on

images of the underlying vasculature at depths of 100 μm and deeper. The intensity profiles in Fig. 2e also show no noticeable intensity loss caused by the metal trace. These results demonstrate that the Smart Dura is applicable to brain functional imaging via multiphoton microscopy, as it can image fluorescent targets as small as neurons under the Smart Dura, and the narrow traces become transparent for the images beyond a certain depth with minimal intensity loss.

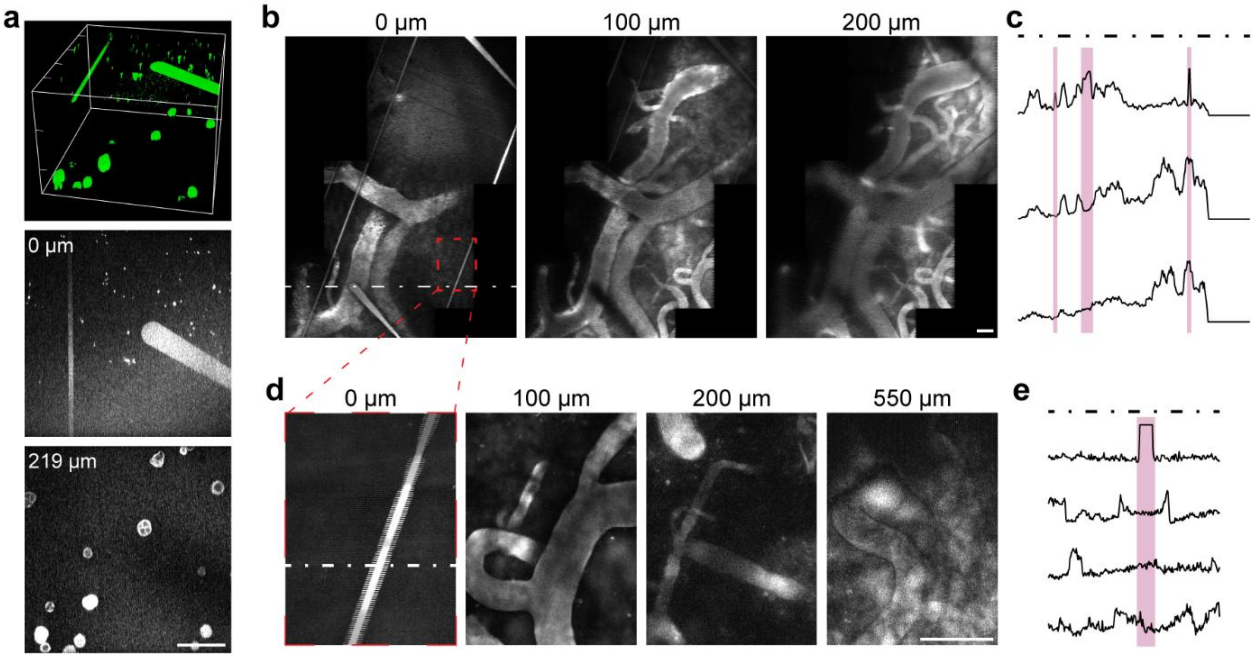

Fig. 2. Multiphoton fluorescent imaging through the Smart Dura. (a) Two-photon imaging of pollen grains placed under the Smart Dura. The electrode is facing downward, which is the same condition as when recording neuronal signals in the brain. The top of a 3D multi-stack image shows the electrode and metal traces (Depth: 0 μm), and the bottom stack shows the pollen grains (Depth: 219 μm). (b) In vivo vascular images at depths of 0, 100, and 200 μm in V1 under the Smart Dura using two-photon microscopy. The image at a depth of 0 μm is the plane focused on the metal traces. (c) Intensity profiles at different depths along the white dashed line shown in the image of 0 μm. The shaded areas indicate where the metal traces pass through. (d) Three-photon images of the vasculatures under the Smart Dura. The images were taken from the area highlighted in a red dashed box in Fig. 2b. (e) Intensity profiles at different depths along the white dashed line shown in the image of 0 μm. The shaded area indicates where the metal trace passes through. Ticks in the 3D images and scale bars in 2D images: 100 μm.

Photochemical ischemic lesioning and OCTA through the Smart Dura

To explore optical manipulation in addition to optical imaging using our Smart Dura, we employed photothrombotic lesioning to induce ischemic stroke. The photothrombotic technique, developed in our recent publication[31], can generate focal ischemic lesions in the NHP cortex photochemically using a photosensitive dye Rose Bengal. To image changes in the vasculature, we performed OCTA before and after stroke induction using a custom-built OCT system[32,33].

We first induced an ischemic lesion in V1 by intravenous administration of Rose Bengal and localized light illumination (Fig. 3a). OCTA images acquired before and after stroke induction (Fig. 3b) show a significant reduction in blood flow centered on the illuminated area. Next, we analyzed stroke-induced changes in neural activity using electrophysiological recordings from Smart Dura. Figure 3c presents gamma band (30-59 Hz) traces of an electrode within the lesion, showing a significant decline in amplitude after stroke. As shown in the heatmaps of Fig. 3d, this decrease in gamma power was prominently observed in the stroke-induced region detected in OCTA images, similar to our previous studies[31,34,35].

To demonstrate that the electrical stimulation can be combined with this optical manipulation, we attempted to replicate our recent work[34,35] on a post-stroke acute stimulation for neuroprotection. Our previous study found an increase in gamma power in the perilesional area at 1-2 hours after stroke, in contrast to the gamma power decrease occurring in the lesion. Such hyperactivation could be suppressed by applying theta-burst electrical stimulation near the lesion. Here, we delivered electrical stimulation 60 minutes after stroke induction. Figure 3e shows the normalized gamma power of pre-stroke, post-stroke, and post-electrical stimulation periods. Consistent with our previous findings, a progressive decrease in gamma power was observed as electrical stimulation continued following the stroke. Taken together, the results suggest that Smart Dura can be integrated with optical illumination and imaging to induce acute stroke, monitor neurological and vascular changes, and even provide therapeutic electrical stimulation.

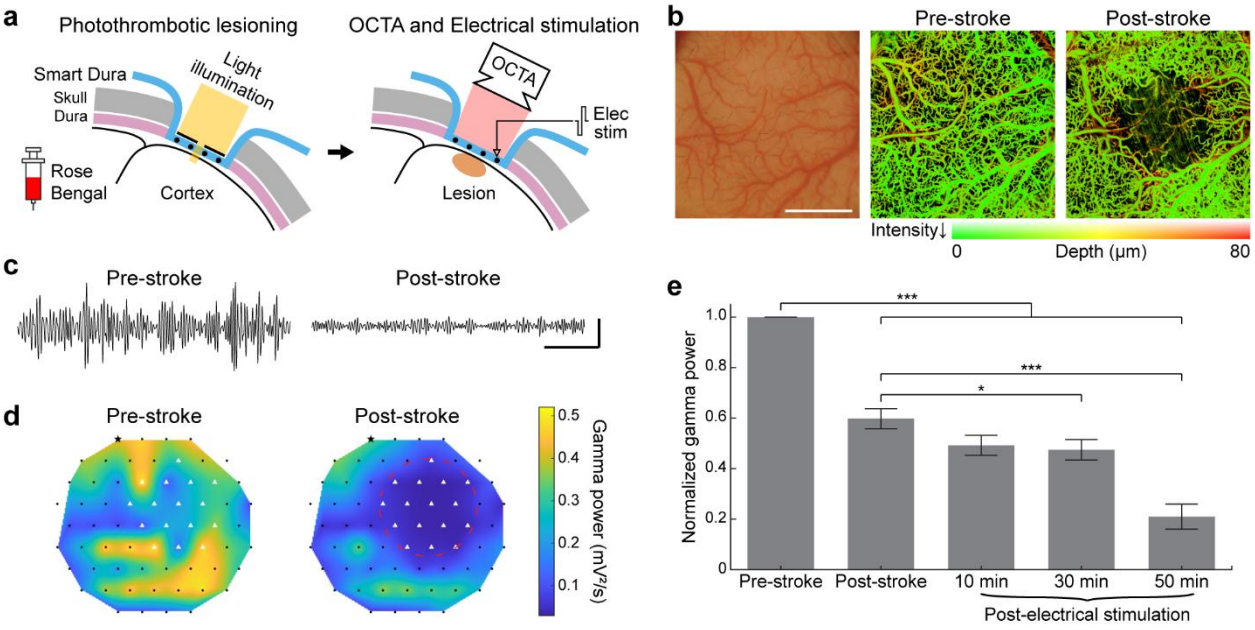

Fig. 3. Photochemical ischemic lesioning and OCTA imaging combined with electrical recording and stimulation of the Smart Dura. (a) Schematics of photothrombotic lesioning through the Smart Dura to induce an ischemic stroke, optical coherence tomography angiography (OCTA) imaging, and neuroprotective electrical

stimulation after stroke. (b) The surface of the V1, covered with the Smart Dura (left). Ischemic stroke was photochemically induced by illuminating a light in the center of the area. OCTA images before (center) and after stroke (right), showing the absence of blood flow in the stroke-induced region. Scale bar: 5 mm. (c) Representative gamma band traces of an electrode in the stroke-induced region before and after the stroke. Scale bar: 500 ms and 50 μV. (d) Heatmaps of gamma power before and after the stroke, showing the power decrease in the stroke-induced region detected in OCTA images. A red circle and white triangles denote the stroke-induced region and the electrodes within the area, respectively. (e) Normalized gamma power of electrodes, not in the stroke-induced region, before and after stroke, and after electrical stimulation. Electrical stimuli were delivered to the electrode marked with a start in Fig. 3d. Repeated measures ANOVA with Bonferroni's post-hoc test. n = 40 electrodes.

Intrinsic signal optical imaging (ISOI) with simultaneous electrophysiology

To assess the feasibility of simultaneous electrophysiological recording and optical functional imaging using our Smart Dura, we used wide-field ISOI, which is an imaging technique to indirectly infer neural activity based on hemodynamic response changes[36]. We imaged evoked responses to visual stimulation via ISOI in V1 of the anesthetized animal while recording neural signals from the same cortical area using the Smart Dura (Fig. 4a). Visual stimuli were presented to either the left or right eye for 4 seconds, and chromatic and achromatic stimuli were randomly delivered. Figure 4b shows representative spectrograms of neural activity at an electrode during chromatic or achromatic visual stimulation. For both stimuli, signal power increased as the stimulus was applied, and such power increase was particularly prominent in the high-gamma (HG) band of 60-150 Hz.

Using intrinsic signals acquired using ISOI, we could create two basic functional maps with high spatial resolution: a color map (Fig. 4c) and an ocular dominance map (Fig. 4d). Color blobs and ocular dominance columns, which are well-known as characteristic features of V1 in macaques, were observed in the color map and ocular dominance map, respectively. To investigate how these color or ocular-specific responses correlated with the neural responses measured by the Smart Dura, we first selected two electrodes that strongly responded to chromatic or achromatic stimuli, respectively. We then quantified the averaged HG power for each electrode and the time course of the intrinsic signal at a pixel near that electrode. The left graph in Fig. 4e shows the HG power of the electrode having a chromatic dominance throughout the visual stimulation. The intrinsic signal response exhibited slower dynamics with a peak delayed by about 3 seconds, but the dominance was consistent. In contrast, the right graph in Fig. 4e presents the electrode that showed overall achromatic dominance in HG power, and a similar trend was observed in the intrinsic signal. In addition to the color dominance, we chose two electrodes that were highly activated in either left or right eye stimulation. As shown in Fig. 4f, comparable ocular dominances were found between HG powers and intrinsic signals. Lastly, we examined the evoked response to visual stimulation before and after stroke. As described above, we induced an ischemic stroke in V1 via a photothrombotic lesioning technique and confirmed that the gamma power of the spontaneous activity significantly decreased after the stroke. Here,

we evaluated the changes in the visual stimulus-evoked responses in HG powers and intrinsic signals caused by stroke induction. Figure 4g shows pre- and post-stroke responses at the electrode and pixel within the stroke region, and both responses almost disappeared after the stroke was induced. On the other hand, in the electrode far from the stroke region (Fig. 4h), HG power and intrinsic signal increase in response to visual stimulation were preserved. These results imply a great potential to integrate neural recordings of the Smart Dura with various functional imaging techniques, thereby obtaining multimodal information with different spatiotemporal resolutions.

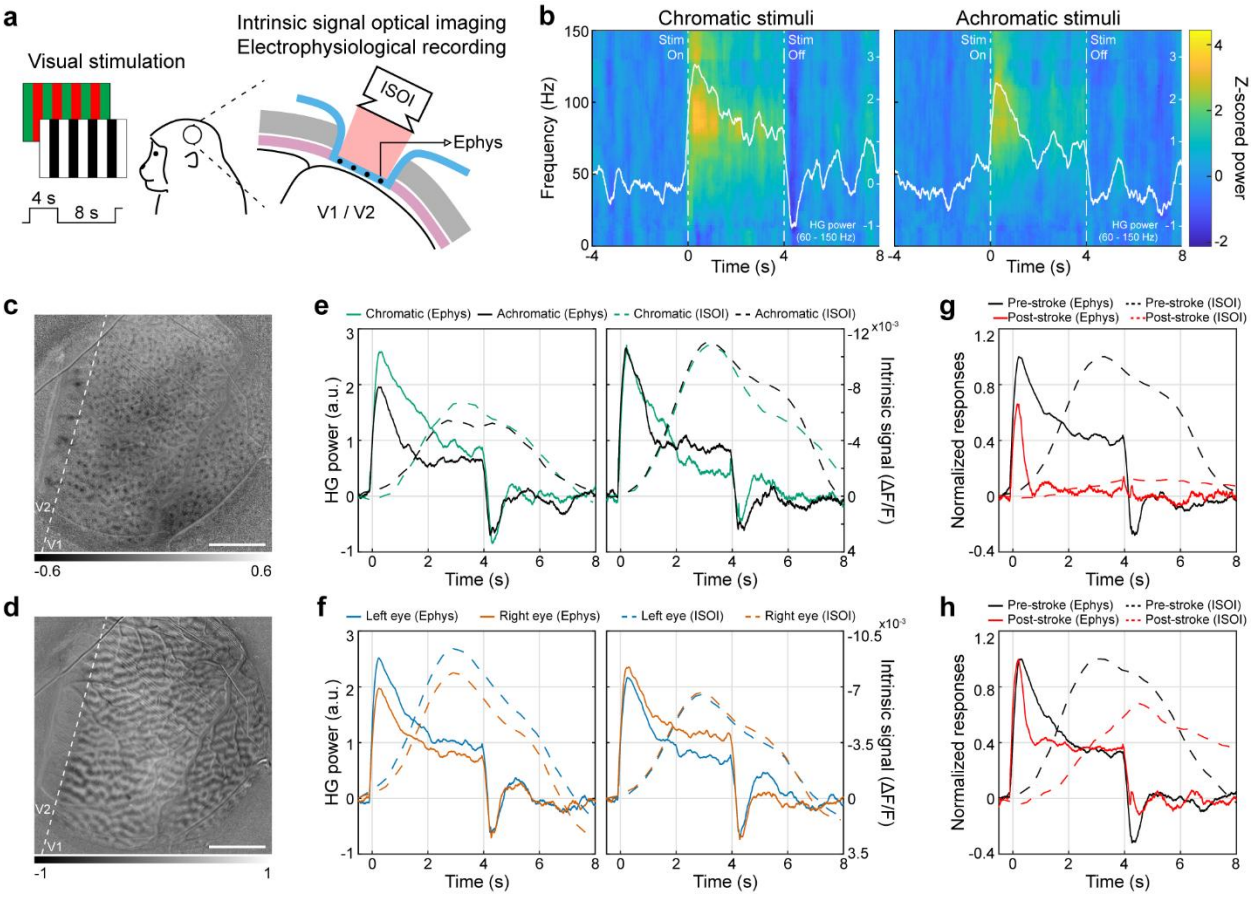

Fig. 4. Intrinsic signal optical imaging through the Smart Dura with simultaneous electrophysiology. (a) Schematics of visual stimulation to the anesthetized animal and simultaneous intrinsic signal optical imaging (ISOI) and electrophysiological recording (Ephys) from V1. (b) Representative spectrograms for an electrode, showing trial-averaged neural responses during chromatic or achromatic visual stimulation. 10 trials for each stimulation. The averaged high-gamma (HG) powers in the 60-150 Hz frequency band are overlaid in white. The stimulation onset occurred at 0 s and lasted 4 seconds. (c) Color map for left eye stimulation, exhibiting color blobs that are color-preferring neuronal clusters, and (d) Ocular dominance map, showing ocular dominance columns (left eye minus right eye). The white dashed line shows the primary and secondary visual cortex (V1/V2) border. Scale bar: 5 mm. (e) Trial-averaged HG power via Ephys and intrinsic signal via ISOI in response to chromatic or achromatic stimuli. 80 trials for each stimulation. The left and right graphs show neural responses of electrodes with the greatest preference for chromatic or achromatic stimuli, respectively. (f) Trial-averaged HG power via Ephys and intrinsic signal via ISOI

in response to left-eye or right-eye stimulation. 160 trials for each stimulation. The left and right graphs show neural responses of electrodes with left-eye or right-eye dominance, respectively. Intrinsic hemodynamic responses were obtained from randomly selected pixels near each electrode. The y-axis for intrinsic signals is drawn in reverse. (g) Normalized responses of Ephys and ISOI before and after stroke at an electrode and pixel in the stroke region. (h) Normalized responses before and after stroke at an electrode and pixel away from the stroke region. 160 trials for each stimulation.

Optogenetic neuromodulation through the Smart Dura

To demonstrate the applicability of our Smart Dura for optogenetic experiments, we performed optogenetic modulation in the awake animal that had widespread expression of an inhibitory opsin Jaws. We infused a red-light-activated Jaws into the posterior parietal cortex (PPC) using convection-enhanced delivery, which enables large-scale viral vector delivery and opsin expression[22,37,38]. At around two years after the initial injection of a red-light-activated opsin Jaws, epifluorescence imaging revealed that there is still distinct opsin/GFP expression at two separate regions over the PPC, as shown by the green regions in Fig. 5a. To activate the opsin, we delivered red-light stimuli (Fig. 5b; 634 nm; 0.9 W/cm^2) through the Smart Dura using a custom-built LED array[39,40] to the entire cortical area. We then recorded neural activity and evaluated power changes in broadband LFPs at frequencies of 1-200 Hz for individual electrodes in the opsin-expressing and opsin-deficient neural regions (Fig. 5c). During the light stimulation, the broadband LFP power significantly increased in the area expressing the opsin, but not in the opsin-deficient region. A time-frequency representation of this differential response between opsin-deficient (Fig. 5d) and opsin-expressing (Fig. 5e) regions shows a power increase in the 20-40 Hz frequency band only for the opsin-expressing region. This localized power increase, selective for opsin-expressing regions, is consistent with findings elaborated on in our previously published work[40] and confirms the ability of the Smart Dura to modulate neural activity and simultaneously record frequency-specific evoked responses.

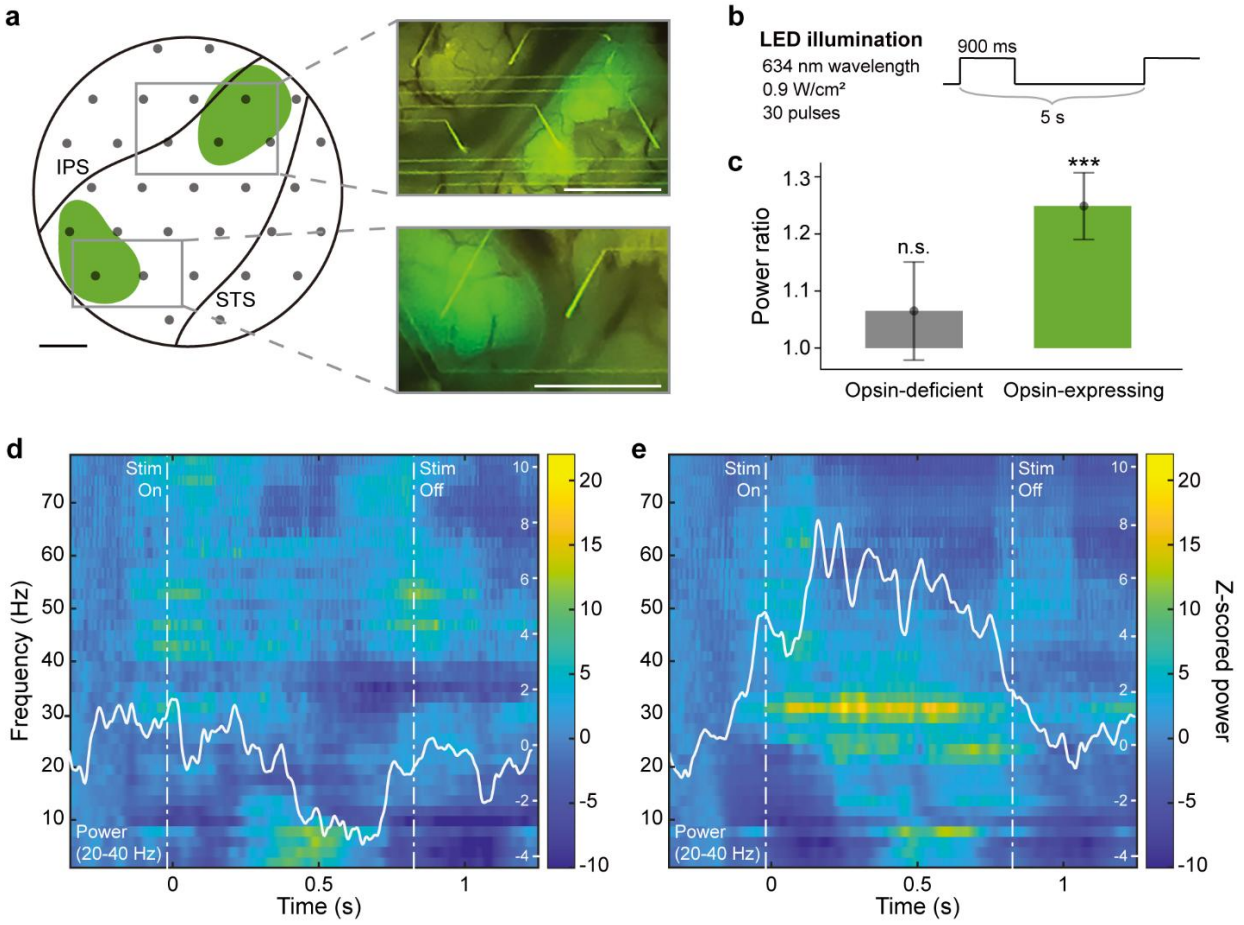

Fig. 5. Characterization of evoked neural response during targeted optogenetic modulation. (a) Optogenetic expression of opsin Jaws and electrode placement of the Smart Dura over the PPC of the awake animal (IPS: intraparietal sulcus. STS: superior temporal sulcus). Green regions indicate locations with strong opsin expression. Insets on the right show optical access and epifluorescence over the two expressing regions at the start of optogenetic experiments. Scale bar: 2.5 mm. (b) Light stimulation pulses. (c) Light-evoked neural responses at individual electrodes in the opsin-deficient region and opsin-expressing region. The broadband LFP (1-200 Hz) power ratio during to before stimulation significantly increased at the opsin-expressing location ($p = 2.34 \times 10^{-5}$; one-sample t-test), whereas the power ratio at the opsin-deficient location was not ($p = 0.157$; one-sample t-test). One-sample t-test. $n = 30$ trials. (d-e) Trial-averaged spectrograms of neural activity during light stimulation at electrodes in the opsin-deficient region and opsin-expressing region, respectively. The light pulse onset occurred at $t = 0$ and lasted 900 ms. For each spectrogram, the averaged power in the 20-40 Hz frequency band is overlaid in white.

Discussion

In this study, we demonstrated the compatibility of our multimodal interface Smart Dura for NHPs with a series of optical imaging and manipulations. In terms of optical imaging applications, both multiphoton microscopy capable of deep brain imaging at the single-cell level, and ISOI with a wide field of view on the surface could be applied to image the cortex through the Smart Dura. As for optical manipulations, optogenetics allowing reversible light-controlled neuromodulation, as well as photothrombotic lesioning that can cause irreversible localized neuronal damage, could be combined with the electrophysiology of the

Smart Dura. The integration of Smart Dura's electrical functionality and optical imaging and manipulations at multiple spatial and temporal scales – from individual neurons to network-wide or from slow calcium signals to fast action potentials – can provide new insight into complementary natures of multiscale information. This enables a comprehensive understanding of brain functions and innovative therapeutic paradigms for neurological disorders, ultimately being applicable and translatable to humans.

Methods

Animal subjects and electrophysiological recording

Animal care and experiments were approved by the University of Washington's Office of Animal Welfare, the Institutional Animal Care and Use Committee, and the Washington National Primate Research Center (WaNPRC). We tested our Smart Dura on two male macaques: *Macaca nemestrina*, 4.8 kg, 4 years was used for the experiments under anesthesia, and *Macaca mulatta*, 12.6 kg, 11 years was used for the awake experiments. The first animal underwent unilateral craniotomy and durotomy with a 25 mm diameter targeting the primary visual cortex (V1) in the left hemisphere. The second animal has a pre-established cranial window overlying the left posterior parietal cortex (PPC)[39,40].

All electrophysiological recordings were performed using a 64-channel Smart Dura, developed in our previous work[18]. The Smart Dura was placed on the surface of the cortex and connected to the Front ends (Nano2+Stim; band-pass filter: 1 Hz-7.5 kHz), interfacing with a Grapevine Nomad processor and Trellis software (Ripple Neuro, UT). Raw signals were digitized at a sampling rate of 30 kHz. Local field potentials (LFPs) were sampled at 1 kHz by low-pass filtering at 250 Hz with notch filters at multiples of 60 Hz. Subsequent signal processing and data analyses were carried out using MATLAB (MathWorks Inc., MA).

Multiphoton imaging

Two- and three-photon imaging were conducted with a multi-photon microscope (MOM; Sutter Instruments, CA) equipped with excitation lasers set to 920 nm and 1300 nm wavelengths, respectively[41]. The laser beam was focused with a 16x (NA = 0.8; Nikon, Japan) or 25x (NA = 1.05; Olympus, Japan) water immersion objective lens. The microscope was controlled by ScanImage software (Vidrio Technologies, VA). For imaging of pollen grains, a microscope slide with mixed pollen grains (B690; Carolina Biological, NC) was utilized and the Smart Dura was located between the objective lens and the sample slide. For in vivo vasculature imaging, the Smart Dura was placed on the V1 surface of the anesthetized animal, and FITC-dextran (50 mg/kg; 50 mg/mL in sterile water; 52471; Sigma-Aldrich) was intravenously injected. A depth of 0 μm for all images is set to the plane focused on the electrodes and

metal traces. 3D image stacking, pseudo-coloring, image stitching, and intensity profile measurements were performed using ImageJ (National Institutes of Health, MD).

Photothrombotic lesioning followed by electrical stimulation

We induced photochemical ischemic lesioning in V1 using the photothrombotic technique[31]. The Smart Dura was placed on the cortical surface and an opaque silicone mask with a 1.5 mm-diameter circular aperture in the center was placed over it. A photoactive dye Rose Bengal (20 mg/kg; 40 mg/mL in saline; 330000; Sigma-Aldrich) was infused intravenously for 5 minutes simultaneously with the start of illumination using a cold white light source (KL 2500 LCD; SCHOTT, UK). Light illumination through the mask aperture lasted for 30 minutes.

We recorded pre-stroke and post-stroke neural activity for 30 and 60 minutes, respectively, and then delivered theta-burst electrical stimuli to an electrode approximately 6.5 mm medial to the lesion center. Electrical stimulation was applied with the same parameters as those used in our previous work[34,35], except that the stimulation amplitude was 30 μA. Between each stimulation block, 2 minutes of spontaneous activity was recorded. The averaged gamma power in the frequency band of 30-59 Hz for each electrode was calculated by squaring the signal and dividing it by its duration. To compare gamma power, we used a repeated measures ANOVA with Bonferroni's post-hoc test. Pairwise comparisons were only performed between pre-stroke and other recording blocks and between post-stroke and post-electrical stimulation recording blocks.

OCTA imaging

We used a custom-built optical coherence tomography (OCT) system for OCT angiography (OCTA) imaging. The prototype is similar to the device, reported in our previous publications[32,33]. Briefly, the system employed a swept-source laser operating at 200 kHz, with a center wavelength of 1310 nm and an optical bandwidth of 100 nm, providing an axial resolution of about 8 μm in tissue. The objective lens (LSM04; Thorlabs Inc., NJ) had a focal length of 54 mm and provided a lateral resolution of about 35 μm. The total beam power incident to the Smart Dura was 5 mW.

The acquisition time of one OCT data volume took 8 seconds. Each data volume covered a 9×9 mm^2 cortical area, rasterized into 500 cross-sectional planes with each plan containing 500 A-scans. Four repeated B-scans were acquired at every individual plane for contrasting blood flow. During the imaging session, five data volumes were consecutively acquired at the center, anterior-medial, anterior-lateral, posterior-lateral, and posterior-medial sections of the cranial window to cover the entire area (i.e., the center and four corners). The system-embedded RGB camera was used to navigate the imaging probe in real-time.

The OCTA image processing was conducted in MATLAB (MathWorks Inc., MA). An eigen-decomposition-based algorithm[42] was first used to contrast the blood flow signal. Then, top-down max-intensity projection was performed to suppress the blood flow volumes onto two-dimensional vascular maps, with pseudo-color encoding to indicate the depth of the vessels. Finally, these individual maps were stitched together to form a larger map covering the entire region.

Visual stimulation

To characterize the neural responses evoked by visual stimuli from electrophysiological recordings, a multitaper spectrogram was generated in a window of 300 ms with 3-ms steps for each trial. Each time-frequency bin was z-scored with respect to the frequency band power 4 seconds before the onset of stimulation. The z-scored spectrograms were averaged across trials, and high-gamma power was obtained from bins 60-150 Hz of the trial-averaged spectrogram.

Optogenetic neuromodulation

During the surgical implantation of a chronic chamber as described in our previous works[39,40], we virally infused a red-light-activated inhibitory opsin Jaws[43] into the PPC using convection-enhanced delivery[22] of viral vector rAAV8-hSyn-Jaws-KGC-GFP-ER2 (UNC Vector Core, NC). The optogenetic experiment demonstrated in this work was performed around 2 years after the initial injection. To test the expression level at different locations over the optical window, we performed epifluorescence imaging of the GFP fluorescence tag through the Smart Dura using a blue light source (440-460 nm excitation; SFA-RB; NIGHTSEA, PA) and a green emission filter (500-560 nm bandpass) attached to a digital camera with 35mm lens (D5300; Nikon, Japan). Each quadrant of the optical window was illuminated sequentially during imaging, and the images were stacked and averaged in Photoshop (Adobe, CA) to improve quality and contrast over the full window.

To activate the opsin by applying light stimulation, an LED array was placed over the Smart Dura, described in detail in our previous publications[39,40]. The array consisted of a 4×4 grid of LEDs emitting light at a wavelength of 634 nm at 0.9 W/cm^2 over the entire cortical area (about 1.0 cm^2). 30 light pulses were delivered every 5 seconds, lasting 900 ms. To remove the photoelectric artifact generated by the light pulse, an electrode recording in saline was subject to the same light stimulation paradigm, and the first three principal components (PCs) of the artifact during the 900 ms of stimulation and 900 ms after stimulation were used to generate two templates of the artifact without neural activity, respectively. Each stimulation pulse in the neural recording was segmented into 900 ms during and 900 ms after stimulation and then projected onto the PC space of the corresponding saline template. The scaled projection of the neural data was then subtracted from the original neural recording to remove the artifact.

To characterize the light-evoked neural response, a multitaper spectrogram with a non-overlapping 50 ms window for each stimulation pulse was used. Each time-frequency bin was z-scored with respect to the frequency band power 500 ms before the onset of stimulation. The time-frequency bins during the 900 ms stimulation were then averaged between 1-200 Hz to calculate the evoked response ratio. The evoked response was considered significant if the power ratio during stimulation was significantly greater ($*p < 0.05$) using a one-sample t-test where the null hypothesis is rejected when the mean is not equal to 1.

Acknowledgments

This work was supported by the National Institute of Neurological Disorders and Stroke of the National Institutes of Health (NIH) R01NS116464, R01NS119395, and U01NS115585, the National Institute of Mental Health of the NIH R01MH125429 and UG3MH126864, the Washington National Primate Research Center P51OD010425 and U42OD011123 from the NIH Office of Research Infrastructure Programs, the Washington Research Foundation, the American Heart Association, the NIH T32 training in theoretical and computational approaches to neural circuits of cognition 1T32MH132518, the Weill Neurohub, the National Institute of Biomedical Imaging and Bioengineering of the NIH EB029365, and the Bertucci Nanotechnology Laboratory at Carnegie Mellon University BNL-78657879.

Competing interests

The authors declare no competing interests.

References

1. Vázquez-Guardado, A., Yang, Y., Bandodkar, A. J. & Rogers, J. A. Recent advances in neurotechnologies with broad potential for neuroscience research. *Nat. Neurosci. 2020 2312* **23**, 1522–1536 (2020).

2. Boyden, E. S., Zhang, F., Bamberg, E., Nagel, G. & Deisseroth, K. Millisecond-timescale, genetically targeted optical control of neural activity. *Nat. Neurosci. 2005 89* **8**, 1263–1268 (2005).

3. Fekete, Z., Zátonyi, A., Kaszás, A., Madarász, M. & Slézia, A. Transparent neural interfaces: challenges and solutions of microengineered multimodal implants designed to measure intact neuronal populations using high-resolution electrophysiology and microscopy simultaneously. *Microsystems Nanoeng. 2023 91* **9**, 1–30 (2023).

4. Cho, Y. U., Lim, S. L., Hong, J. H. & Yu, K. J. Transparent neural implantable devices: a comprehensive review of challenges and progress. *npj Flex. Electron. 2022 61* **6**, 1–18 (2022).

5. Ramezani, M., Ren, Y., Cubukcu, E. & Kuzum, D. Innovating beyond electrophysiology through multimodal neural interfaces. *Nat. Rev. Electr. Eng. 2024 21* **2**, 42–57 (2024).

6. Liu, X. *et al.* Multimodal neural recordings with Neuro-FITM uncover diverse patterns of cortical–hippocampal interactions. *Nat. Neurosci. 2021 246* **24**, 886–896 (2021).

7. Renz, A. F. *et al.* Opto-E-Dura: A Soft, Stretchable ECoG Array for Multimodal, Multiscale Neuroscience. *Adv. Healthc. Mater.* **9**, 2000814 (2020).

8. Thunemann, M. *et al.* Deep 2-photon imaging and artifact-free optogenetics through transparent graphene microelectrode arrays. *Nat. Commun. 2018 91* **9**, 1–12 (2018).

9. Zhang, J. *et al.* Stretchable Transparent Electrode Arrays for Simultaneous Electrical and Optical Interrogation of Neural Circuits in Vivo. *Nano Lett.* **18**, 2903–2911 (2018).

10. Donahue, M. J. *et al.* Multimodal Characterization of Neural Networks Using Highly Transparent Electrode Arrays. *eNeuro* **5**, (2018).

11. Kunori, N. & Takashima, I. A transparent epidural electrode array for use in conjunction with optical imaging. *J. Neurosci. Methods* **251**, 130–137 (2015).

12. Zátonyi, A. *et al.* Functional brain mapping using optical imaging of intrinsic signals and simultaneous high-resolution cortical electrophysiology with a flexible, transparent microelectrode array. *Sensors Actuators B Chem.* **273**, 519–526 (2018).

13. Richner, T. J. *et al.* Optogenetic micro-electrocorticography for modulating and localizing cerebral cortex activity. *J. Neural Eng.* **11**, 016010 (2014).

14. Park, D. W. *et al.* Graphene-based carbon-layered electrode array technology for neural imaging and optogenetic applications. *Nat. Commun. 2014 51* **5**, 1–11 (2014).

15. Cho, Y. U. *et al.* Ultra-Low Cost, Facile Fabrication of Transparent Neural Electrode Array for Electrocorticography with Photoelectric Artifact-Free Optogenetics. *Adv. Funct. Mater.* **32**, 2105568 (2022).

16. O'Shea, D. J. *et al.* The need for calcium imaging in nonhuman primates: New motor neuroscience and brain-machine interfaces. *Exp. Neurol.* **287**, 437–451 (2017).

17. Belloir, T. *et al.* Large-scale multimodal surface neural interfaces for primates. *iScience* **26**, 105866 (2023).

18. Vargo, S. M. *et al.* Smart Dura: A Monolithic Optoelectrical Surface Array for Neural Interfacing with Primate Cortex. *Int. IEEE/EMBS Conf. Neural Eng. NER* **2023-April**, (2023).

19. Arieli, A., Grinvald, A. & Slovin, H. Dural substitute for long-term imaging of cortical activity in behaving monkeys and its clinical implications. *J. Neurosci. Methods* **114**, 119–133 (2002).

20. Slovin, H., Arieli, A., Hildesheim, R. & Grinvald, A. Long-term voltage-sensitive dye imaging reveals cortical dynamics in behaving monkeys. *J. Neurophysiol.* **88**, 3421–3438 (2002).

21. Ruiz, O. *et al.* Optogenetics through windows on the brain in the nonhuman primate. *J. Neurophysiol.* **110**, 1455–1467 (2013).

22. Yazdan-Shahmorad, A. *et al.* A Large-Scale Interface for Optogenetic Stimulation and Recording in Nonhuman Primates. *Neuron* **89**, 927–939 (2016).

23. Arieli, A., Grinvald, A. & Slovin, H. Dural substitute for long-term imaging of cortical activity in behaving monkeys and its clinical implications. *J. Neurosci. Methods* **114**, 119–133 (2002).

24. Slovin, H., Arieli, A., Hildesheim, R. & Grinvald, A. Long-term voltage-sensitive dye imaging reveals cortical dynamics in behaving monkeys. *J. Neurophysiol.* **88**, 3421–3438 (2002).

25. Ruiz, O. *et al.* Optogenetics through windows on the brain in the nonhuman primate. *J. Neurophysiol.* **110**, 1455–1467 (2013).

26. Khodagholy, D. *et al.* NeuroGrid: recording action potentials from the surface of the brain. *Nat. Neurosci. 2015 182* **18**, 310–315 (2014).

27. Xu, C., Nedergaard, M., Fowell, D. J., Friedl, P. & Ji, N. Multiphoton fluorescence microscopy for in vivo imaging. *Cell* **187**, 4458–4487 (2024).

28. Kim, T. H. & Schnitzer, M. J. Fluorescence imaging of large-scale neural ensemble dynamics. *Cell* **185**, 9–41 (2022).

29. Horton, N. G. *et al.* In vivo three-photon microscopy of subcortical structures within an intact mouse brain. *Nat. Photonics 2013 73* **7**, 205–209 (2013).

30. Ouzounov, D. G. *et al.* In vivo three-photon imaging of activity of GCaMP6-labeled neurons deep in intact mouse brain. *Nat. Methods 2017 144* **14**, 388–390 (2017).

31. Khateeb, K. *et al.* A versatile toolbox for studying cortical physiology in primates. *Cell Reports Methods* **2**, 100183 (2022).

32. Xie, Z., Shi, Y., Marmin, A. & Wang, R. K. Investigation of the Effect of Compression Pressure in Contact OCT Imaging on the Measurement of Epidermis Thickness. *J. Biophotonics* e202400289 (2024) doi:10.1002/JBIO.202400289.

33. Deegan, A. J., Lu, J., Sharma, R., Mandell, S. P. & Wang, R. K. Imaging human skin autograft integration with optical coherence tomography. *Quant. Imaging Med. Surg.* **11**, 78496–78796 (2021).

34. Zhou, J. *et al.* Neuroprotective Effects of Electrical Stimulation Following Ischemic Stroke in Non-Human Primates. *Proc. Annu. Int. Conf. IEEE Eng. Med. Biol. Soc. EMBS* **2022-July**, 3085–3088 (2022).

35. Zhou, J., Khateeb, K. & Yazdan-Shahmorad, A. Early Intervention with Electrical Stimulation Reduces Neural Damage After Stroke in Non-human Primates. *bioRxiv* 2023.12.18.572235 (2023) doi:10.1101/2023.12.18.572235.

36. Grinvald, A., Lieke, E., Frostig, R. D., Gilbert, C. D. & Wiesel, T. N. Functional architecture of cortex revealed by optical imaging of intrinsic signals. *Nat. 1986 3246095* **324**, 361–364 (1986).

37. Khateeb, K., Griggs, D. J., Sabes, P. N. & Yazdan-Shahmorad, A. Convection Enhanced Delivery of Optogenetic Adeno-associated Viral Vector to the Cortex of Rhesus Macaque Under Guidance of Online MRI Images. *J. Vis. Exp.* (2019) doi:10.3791/59232-V.

38. Griggs, D. J. *et al.* Improving the Efficacy and Accessibility of Intracranial Viral Vector Delivery in Non-Human Primates. *Pharmaceutics* **14**, 1435 (2022).

39. Griggs, D. J. *et al.* Demonstration of an Optimized Large-scale Optogenetic Cortical Interface for Non-human Primates. *Proc. Annu. Int. Conf. IEEE Eng. Med. Biol. Soc. EMBS* **2022-July**, 3081–3084 (2022).

40. Griggs, D. J. *et al.* A large-scale optogenetic neurophysiology platform for improving accessibility in NHP behavioral experiments. *bioRxiv* 2024.06.25.600719 (2024) doi:10.1101/2024.06.25.600719.

41. Takasaki, K., Abbasi-Asl, R. & Waters, J. Superficial Bound of the Depth Limit of Two-Photon Imaging in Mouse Brain. *eNeuro* **7**, (2020).

42. Yousefi, S., Zhi, Z. & Wang, R. K. Eigendecomposition-based clutter filtering technique for optical microangiography. *IEEE Trans. Biomed. Eng.* **58**, 2316–2323 (2011).

43. Chuong, A. S. *et al.* Noninvasive optical inhibition with a red-shifted microbial rhodopsin. *Nat. Neurosci. 2014 178* **17**, 1123–1129 (2014).